

Combining Anatomical and Functional Networks for Neuropathology Identification: A Case Study on Autism Spectrum Disorder

Sarah Itani^{a,b,*}, Dorina Thanou^c

^a*Fund for Scientific Research - FNRS (F.R.S.-FNRS), Brussels, Belgium*

^b*Department of Mathematics and Operations Research, Faculty of Engineering, University of Mons, Mons, Belgium*

^c*Swiss Data Science Center, EPFL and ETH Zurich, Switzerland*

Abstract

While the prevalence of Autism Spectrum Disorder (ASD) is increasing, research towards the definition of a common etiology is still ongoing. In this regard, modern machine learning and network science pave the way for a better understanding of the pathology and the development of diagnosis aid systems. At the same time, the culture of data sharing heads favorably in that direction, with the availability of large datasets such as the Autism Brain Imaging Data Exchange (ABIDE) one. The present work addresses the classification of neurotypical and ASD subjects by combining knowledge about both the anatomy and the functional activity of the brain. In particular, we model the brain structure as a graph, and the time-varying resting-state functional MRI (rs-fMRI) signals as values that live on the nodes of that graph. We then borrow tools from the emerging field of Graph Signal Processing (GSP) to build features related to the frequency content of these signals. In order to make these features highly discriminative, we apply an extension of the Fukunaga-Koontz transform. Finally, we use these new markers to train a decision tree, an interpretable classification scheme, which results in a final diagnosis aid model. Interestingly,

*Corresponding author. University of Mons, Department of Mathematics and Operations Research, Rue de Houdain, 9, 7000 Mons, Belgium.

Email addresses: sarah.itani@umons.ac.be (Sarah Itani), dorina.thanou@epfl.ch (Dorina Thanou)

the resulting decision tree outperforms state-of-the-art methods on the ABIDE dataset. Moreover, the analysis of the predictive markers reveals the influence of the frontal and temporal lobes in the diagnosis of the disorder, which is in line with previous findings in the literature of neuroscience. Our results indicate that exploiting jointly structural and functional information of the brain can reveal important information about the complexity of the neuropathology.

Keywords: Graph signal processing; fMRI; Machine learning; Decision trees; Autism spectrum disorder.

1. Introduction

Understanding the human brain in all its complexity has always been one of the greatest challenges of science in general, not only limited to the medical research. Despite the undeniable progress made in the domain, some neuropathologies, such as Autism Spectrum Disorder (ASD), are characterized by the absence of a commonly defined etiology (Maximo et al., 2014). People with ASD manifest recurring behavioral patterns; they present impairments in language and communication which impede their social interactions (Autism Speaks, 2018). With the growing prevalence of ASD, especially in children, it becomes urgent to determine the neurophysiological bases of the disorder, and use this knowledge for an early and objective diagnosis. Towards that direction, data-driven techniques are expected to shed some light on explainable and interpretable markers that capture the complexity of the neuropathology (Kassraian-Fard et al., 2016) and reveal interconnected patterns on the brain activation that are related to the causes of the disease.

While there is no consensus on the etiology of ASD, it is commonly accepted by the research community that the disorder can be explained by studying the brain network connectivity (Uddin et al., 2013) i.e., the interaction between brain regions. In particular, two types of connectivity have been studied exhaustively: the functional and the structural connectivity. On the one hand, *functional connectivity* (FC) measures the level of interaction between brain

components as the correlation between the related time-series (Sporns, 2013), e.g., Bold-Oxygen Level Dependent (BOLD) fluctuations. The latter can be derived from resting-state functional Magnetic Resonance Imaging (rs-fMRI), a technique which has achieved tremendous success over the last years (Cheng et al., 2017) mainly because it is fast, and task-free (Kassraian-Fard et al., 2016). The functional connectivity is then defined as a pairwise measure of similarity between activity patterns of brain regions, which do not necessarily have a physical connection. On the other hand, *structural connectivity* (SC) is related to the presence of anatomical links between brain components (Sporns, 2013). It thus captures the complex, topological structure of the brain. The structural connectivity is usually measured through Diffusion Tensor Imaging (DTI). Functional and structural connectivity are two equally important sources of information that nevertheless are fundamentally different: (1) they evolve on different time scales, i.e., FC evolves over the very short term while SC evolves over the long term, and (2) they are not necessarily co-existing between a pair of brain zones (Sporns, 2013; Vissers et al., 2012).

Data acquired using these techniques can be analyzed in terms of network structure to reveal organizing principles of the brain that are prevalent in ASD patients through machine learning and statistical approaches (Rane et al., 2015; Kana et al., 2014; Maximo et al., 2014; Uddin et al., 2013; Vissers et al., 2012). In that respect, Chen et al. (2016) investigated resting-state FC in ASD over two frequency bands, namely the SLOW-4 (0.01-0.027 Hz) and SLOW-5 (0.027-0.073 Hz) bands. The FC values were used to train a Support Vector Machine (SVM) classifier. Interestingly, most of the discriminative features were located in the SLOW-4 band. Besides, the analysis of the classification weights showed that the connections of the thalamus are the most discriminative. The work of Goch et al. (2014) used structural network features such as the clustering coefficient and the betweenness centrality to achieve the classification of typically developing and ASD subjects through SVM. The achieved accuracy suggested the relevance of these structural features to understand the pathology. These findings were confirmed by Tolan & Isik (2018), who computed graph measures

on both fMRI and DTI-based networks at global (e.g., diameter, modularity) and nodal levels (e.g., eccentricity, path length). These features were then used to achieve successful predictions through ensemble classification models consisting of SVM, decision tree, and K-nearest neighbor classifiers. Finally, a few studies have considered the joint analysis of both FC and SC, in quest of common functional and structural patterns of (hypo- or hyper-) connectivity in given brain areas (Ray et al., 2014; Mueller et al., 2013; Nair et al., 2013; Uddin et al., 2013). Such an example is the statistics-based study of Mueller et al. (2013), who evidenced common functional and structural impairments in the right temporo-parietal junction area, the left frontal lobe, and the bilateral superior temporal gyrus.

Given the complex nature of the brain and the paramount importance of both functional and structural connectivity, in this work, we combine both sources of information by going beyond their simple embedding. We are actually interested in the extraction of some discriminative information related to the association of both forms of connectivity. In particular, we borrow tools from the emerging framework of Graph Signal Processing (GSP) (Ortega et al., 2018; Shuman et al., 2013), and extend them further, in order to adapt to the ASD case. GSP addresses the challenging problem of analyzing data living on an irregular domain, that can be naturally represented by a graph (e.g., structural brain connectivity). The data lying on the nodes of the graph are considered as signals (e.g., fMRI time-series) that have a strong dependency on the graph topology. Indeed, GSP allows to integrate both structural and functional brain data by studying the interplay between graphs and signals on graphs. Recently, it has been used in analyzing functional brain imaging for the study of cognitive flexibility (Medaglia et al., 2018) and motor skill (Huang et al., 2016) with very promising results.

In this paper, we apply the GSP framework to classify neuroimaging data that are derived from ASD patients. Within this context, the graph consists of a set of brain regions of interest, i.e., graph nodes, that are connected based on the structural distance between them. The BOLD fluctuations observed

on the graph are treated as signals residing on its vertices. We then study the frequency behavior of the BOLD signals by computing their Graph Fourier transform (GFT). The time-varying GFT coefficients are then merged into a single connectivity matrix, from which we compute discriminative graph frequency patterns, by using an extension of the Fukunaga-Koontz transform. To eventually separate ASD from neurotypical subjects, we use these features to train a simple decision tree, an interpretable classification scheme which results in a final diagnosis aid model. The contributions of our study are summarized as follows.

- (1) We address a question which remains open in the light of the current scientific knowledge, namely the relationship between the structural and functional connectivity in ASD subjects (Uddin et al., 2013). For such a purpose, we propose a unified framework that allows to jointly combine the temporal, structural, and functional dimensions of brain data, and highlights discriminative patterns which allow to both explain and predict ASD.
- (2) We show that ASD subjects can be predicted based on frequency patterns on the structural graph that are sophisticated, while remaining interpretable. In that respect, we extend the GSP framework by proposing a way of discriminating time-series in the graph Fourier domain. Indeed, our results suggest that the differences between the ASD and control subjects cannot be attributed to specific graph frequency bands, i.e., typically low, middle and high bands (Medaglia et al., 2018). At the same time, our discriminative patterns can be classified by a simple and interpretable decision tree without the necessity of using more complex classification schemes that are difficult to interpret (e.g., deep learning). This facilitates to a certain extent the interpretation of the predicted results.
- (3) In terms of prediction accuracy, our framework outperforms other state-of-the-art methods that are based on either the spatial or the functional connectivity, i.e., the Graph Fourier Transform - GFT (Ortega et al.,

2018) and the Spatial Filtering Method - SFM (Subbaraju et al., 2017).

Moreover, the interpretation of the results confirms previous findings of the neuroscience literature for the ASD case.

The remainder of the paper is structured as follows. First, in Sec. 2 we briefly describe the necessary tools that are needed to build our framework which is then described in detail. Then, we describe our experimental protocol in Sec. 3. We expose our results in Sec. 4, followed by their interpretation in Sec. 5. Finally, we conclude the paper in Sec. 6.

2. Materials and methods

In this section, we first briefly review a few tools that are important for building our framework. In particular, we present the notation that is used in the remainder of the paper (Subsec. 2.1). Then, we recall basic definitions related to graphs and the representation of signals on graphs, with a strong emphasis on the Graph Fourier Transform (Subsec. 2.2). Moreover, we review the Spatial Filtering Method (Subsec. 2.3) which, to the best of our knowledge, is the closest approach to ours in terms of classification of ASD patients. Finally, we present our framework for graph-based classification of the BOLD signals (Subsec. 2.4).

2.1. Settings and notations

The classification problem that we tackle in this work consists of two classes: (i) NeuroTypical (NT), and (ii) ASD subjects. We denote by

- n_T , the total number of subjects;
- n_A , the total number of ASD subjects;
- n_N , the total number of NeuroTypical (NT) subjects.

Blood Oxygen Level Dependent (BOLD) signals are available for each subject. Each BOLD signal is an r -dimensional vector, where each component corresponds to a brain Region Of Interest (ROI). The brain parcellation in ROI is

usually defined by an atlas, which is the AAL90 atlas in this case (Tzourio-Mazoyer et al., 2002). The BOLD signals per subject consist of time-series, where each component is measured at different points in times. For each subject i ($i = \{1, \dots, n_T\}$), we denote by:

- T_i , the number of time-points in the BOLD signals;
- \mathbf{X}_i , the $r \times T_i$ matrix of BOLD time-series, centered at their mean.

2.2. Graph-based representation of brain signals

We model the structure of the brain as an undirected, weighted graph \mathcal{G} , where the set of nodes ν correspond to the brain regions of interest. The edges of the graph are defined by connecting close ROIs in terms of their topological distance in the brain. In particular, we define the weight A_{uv} between two nodes u, v of a brain graph \mathcal{G} as the inverse of the distance d_{uv} between the two nodes (i.e., regions of interest). Thus, the adjacency matrix A is such that:

$$A_{uv} = d_{uv}^{-1} \quad \text{and} \quad A_{uu} = 0 \quad \text{for} \quad u, v = 1, \dots, r.$$

For each node, we keep only its K nearest neighbors, while ensuring that the final graph is symmetric. The final adjacency matrix is computed as:

$$\mathbf{A}' = \frac{\mathbf{A} + \mathbf{A}^T}{2}. \tag{1}$$

For the sake of simplicity, in what follows, we denote this matrix as \mathbf{A} . The nearest-neighbor strategy used to connect the brain graph is a good proxy for approximating the brain topology, that is widely adopted in the literature (Alexander-Bloch et al., 2012; Bullmore & Sporns, 2009).

We model the time-varying BOLD signals as graph signals that live on the vertices of the graph. In other words, the graph signal at a specific time instance is a vector of r values, which corresponds to a column vector of the matrix \mathbf{X}_i (cf. Subsec. 2.1). The spectral domain representation can reveal significant information about the characteristics of those signals. In particular, the Graph Fourier Transform (GFT) provides a frequency analysis of the signals that reside

on the graph, that is based on the graph Laplacian operator. The combinatorial Laplacian operator (Shuman et al., 2013) is defined as $\mathbf{L} = \mathbf{D} - \mathbf{A}$ where \mathbf{A} is the graph adjacency matrix (see eq. 1) and \mathbf{D} is a diagonal matrix including the degree of each node, i.e., $D_{kk} = \sum_j A_{kj}$. As defined above, the graph Laplacian L has interesting mathematical properties (Von Luxburg, 2007):

- \mathbf{L} is symmetric and positive semi-definite.
- \mathbf{L} has orthonormal eigenvectors \mathbf{V} .
- \mathbf{L} has positive real eigenvalues Λ .
- \mathbf{L} has its smallest eigenvalue equal to zero, and the corresponding eigenvector is constant.

If the graph is fully connected, \mathbf{L} has a single zero eigenvalue and the corresponding eigenvector is constant. Otherwise, there are as many zero eigenvalues as there are disconnected components in the graph.

The eigenvectors of the Laplacian operators can be used to perform an harmonic analysis of signals that live on the graph, and the corresponding eigenvalues carry a notion of frequency (Shuman et al., 2013). Indeed, the eigenvectors of the Laplacian consist of the Fourier basis that can be used for analyzing graph signals. Fig. 1 shows the Graph Fourier modes of a 5-nearest neighbor brain graph. From (a) to (f), we present different frequency modes, in ascending order of eigenvalues, thus graph frequencies. The eigenvectors associated with low eigenvalues (i.e., low frequency) are smooth on the graph (i.e., they are changing slowly across nodes that are connected by an edge). Mode (a) corresponds to a constant graph signal. The second eigenvector of \mathbf{L} , illustrated by (b), is associated with a low evolution of the graph signal.

We study the BOLD time-series \mathbf{X}_i related to a patient i in the frequency domain, through their projection on the eigenvectors of a Laplacian matrix, i.e.,

$$\hat{\mathbf{X}}_i = \mathbf{V}^T \mathbf{X}_i. \quad (2)$$

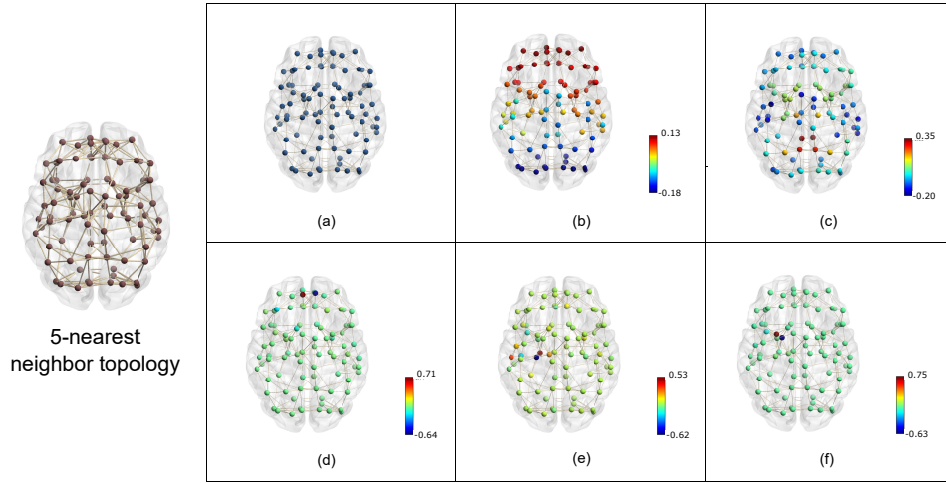


Figure 1: Graph Fourier (GF) basis: illustration on a 5-nearest neighbor topology, consisting of 90 nodes (Tzourio-Mazoyer et al., 2002). The GF modes (or frequencies) presented from (a) to (f) correspond to modes 1, 2, 10, 70, 75 and 90 respectively. The color represents the intensity of the signal (eigenvector of the Laplacian) on the graph. The highest the GF mode, the more fluctuating the signal values on neighboring nodes.

The columns of \hat{X}_i thus correspond to the GFT coefficients for each frequency mode, at a given instance of time.

In the literature, the GFT was previously considered for the analysis and classification of BOLD signals extracted from fMRI data. On the one hand, recent studies achieved the decomposition of signals into three components (low, medium and high frequency) in order to find patterns which are statistically significant to characterize cognitive flexibility (Medaglia et al., 2018) and motor skill (Huang et al., 2016). On the other hand, Wang et al. (2018) suggested that GFT coefficients are not sufficient classification patterns, though used as inputs of a high-performing algorithm such as SVM. The work of Ktena et al. (2018) showed that GFT coefficients have a certain discriminating power when they are embedded within more complex patterns. These are developed through deep learning architectures such as convolutional neural networks.

These findings suggest that the discriminative information brought by the

time-varying GFT coefficients might be hidden in complex patterns. Thus, the challenge remains to discover these complex patterns, and at the same time, insure a certain level of *interpretability* of these patterns, i.e., the ability for a pattern to be understood by humans, and more particularly clinicians in the context of medical data (Itani et al., 2019; Doshi-Velez & Kim, 2017).

2.3. Spatial filtering method

A recent work that is closely related and inspired our framework is the Spatial Filtering Method (SFM) introduced by Subbaraju et al. (2017) as an extension of the Fukunaga-Koontz Transform (FKT) (Fukunaga, 2013; Fukunaga & Koontz, 1970) to the classification of ASD patients. The method addresses the two-class classification problem, by projecting the time-series of the instances in a space defined by the FKT such that they are distinctively separable.

We summarize below the main steps of SFM.

1. A connectivity matrix is computed for each patient i as the covariance of the centered BOLD signals \mathbf{X}_i , normalized by its trace.
2. The connectivity matrices are averaged over all the patients and over the ASD and NT populations distinctively. This operation results in the mean connectivity matrices $\bar{\mathbf{C}}$, $\bar{\mathbf{C}}^{\mathbf{A}}$ and $\bar{\mathbf{C}}^{\mathbf{N}}$ respectively.
3. The eigen-decomposition of the mean covariance matrix is computed as $\bar{\mathbf{C}} = \mathbf{B}\chi\mathbf{B}^T$, which allows to compute the whitening transform as:

$$\mathbf{W} = \chi^{-1/2}\mathbf{B}^T. \quad (3)$$

This operation consists of rotating and re-scaling the data such that they have an identity covariance matrix.

4. Whitening is applied on matrices $\bar{\mathbf{C}}^{\mathbf{A}}$ and $\bar{\mathbf{C}}^{\mathbf{N}}$. Let us denote the resulting whitened matrices as $\bar{\mathbf{C}}^{\mathbf{A}'}$ and $\bar{\mathbf{C}}^{\mathbf{N}'}$. Their simultaneous diagonalization is such that their eigenvalues sum to one on their common set of eigenvectors ψ .

5. The SFM projection matrix is computed as:

$$\mathbf{P}_{\text{SFM}} = \boldsymbol{\psi}^{\text{T}} \cdot \mathbf{W}.$$

6. Finally, each patient’s time-series X_i are projected on the new space:

$$\mathbf{Z}_i^{\text{SFM}} = \mathbf{P}_{\text{SFM}} \cdot \mathbf{X}_i. \tag{4}$$

The simultaneous eigenvalue decomposition of the ASD and NT data is the key element of SFM. Actually, the complementary achieved between the class eigenvalues on the common set of eigenvectors makes possible the separation of the data. Indeed, in the new space, each class is associated with a set of dimensions along which the variance of the related instances is significantly high, and low with respect to the instances of the other class. The variances of the projected data in this new space may thus be used as input features of a classifier. Furthermore, the method achieves dimensionality reduction, by considering the subspace constituted of the most significant dimensions for each class. This space is defined by selecting the dimensions associated to m highest eigenvalues for each class. As a result, the final subspace consists of $2m$ dimensions.

Finally, the analysis of matrix P_{SFM} allows to raise the brain regions whose activity influence significantly the distinction between both classes. SFM is intended to extract discriminative features based on the covariance matrix, which is a way of approximating the functional connectivity of the BOLD signals. As a result, SFM can point out regions whose activity differs significantly between the ASD and NT groups. However, it does not take into account the topology of the brain, i.e., the structural connectivity of the ROIs.

We believe that adding the structural information to the SFM framework can provide more insight on the behavior of the brain in ASD patients. This is the motivation of the framework that we propose in the next section.

2.4. Combining anatomical and functional networks for classification of BOLD signals

We propose a framework that handles simultaneously the structural and functional connectivity of the BOLD signals to extract discriminative patterns

in the graph spectral domain. For such a purpose, our framework builds on both GFT and SFM that were described in the previous subsections (cf. Sec. 2.2 and 2.3). In short, our approach consists of three steps. First, we merge the functional, structural and temporal dimensions of the BOLD time-series. This results in a set of three averaged covariance matrices corresponding to (i) the ASD subjects, (ii) the NT subjects, (iii) the whole set of subjects. These covariance matrices are then used to find a subspace where we can extract discriminative features in order to eventually perform the classification of ASD and NT subjects.

2.4.1. Merging function, structure, and temporality

The first step of our method consists in studying the frequency behavior of the signals on the graph, by computing the GFT coefficients of each subject’s BOLD time-series, using Eq. 2. Projecting the signals in the graph Fourier domain can be considered as a way of decorrelating the signal in that basis. The resulting $r \times T_i$ matrix, denoted as \hat{X}_i , contains the GFT coefficients varying over time for each of the r frequency modes. In order to understand the variation of each GFT coefficient over time, we normalize the GFT coefficients at a specific instance of time, in such a way that the relative importance of each frequency component is revealed. More specifically, we normalize the columns of \hat{X}_i by subtracting the mean of each column and dividing by its energy i.e., the $L2$ norm (see Appendix A.1, Eq. A.1). The resulting matrices are denoted by \mathbf{Y}_i . In order to reveal some frequency patterns of the time-series in the graph Fourier domain, we merge the normalized GFT coefficients over time. We achieve that by computing an approximation of the sample covariance matrix, that is given by:

$$\mathbf{S}_i = \frac{\mathbf{Y}_i \mathbf{Y}_i^T}{\text{tr}(\mathbf{Y}_i \mathbf{Y}_i^T)}. \quad (5)$$

Indeed, if we were to compute a sample covariance matrix in the proper sense of the term, we would have to subtract the mean of the normalized GFT coefficients over the time. Such an operation would lead to losing the benefits of normalizing the GFT coefficients column-wise, i.e., focusing on their relative difference. To

maintain this meaningful interpretation of the columns, we compute the pairwise joint expectancy of the GFT coefficients, which results in an estimation of the covariance matrix \mathbf{S}_i . As shown in [Appendix A.1](#), this matrix is also positive semi-definite. The mean joint expectancy matrix over the whole set of patients is computed as:

$$\bar{\mathbf{S}} = \frac{1}{n_T} \sum_{i=1}^{n_T} \frac{\mathbf{Y}_i \mathbf{Y}_i^T}{\text{tr}(\mathbf{Y}_i \mathbf{Y}_i^T)}. \quad (6)$$

The mean joint expectancy matrices $\bar{\mathbf{S}}^A$ and $\bar{\mathbf{S}}^N$ for all ASD and NT patients respectively are:

$$\bar{\mathbf{S}}^A = \frac{1}{n_A} \sum_{i=1}^{n_A} \mathbf{S}_i \quad \text{and} \quad \bar{\mathbf{S}}^N = \frac{1}{n_N} \sum_{j=1}^{n_N} \mathbf{S}_j.$$

Combining the two last equations, it follows that:

$$\bar{\mathbf{S}} = \frac{n_A}{n_T} \cdot \bar{\mathbf{S}}^A + \frac{n_N}{n_T} \cdot \bar{\mathbf{S}}^N = \frac{n_A}{n_T} \bar{\mathbf{S}}^A + \left(1 - \frac{n_A}{n_T}\right) \cdot \bar{\mathbf{S}}^N. \quad (7)$$

For the remainder of the development, we denote by α_A and α_N respectively, the factors $\frac{n_A}{n_T}$ and $\frac{n_N}{n_T}$, and with $\alpha_N = 1 - \alpha_A$. Eq. 7 can be reformulated as:

$$\bar{\mathbf{S}} = \alpha_A \bar{\mathbf{S}}^A + \alpha_N \bar{\mathbf{S}}^N. \quad (8)$$

The mean joint expectancy matrix is thus expressed as a positive linear combination of both mean joint expectancy matrices of ASD and NT subjects.

At the end of this first stage, we have merged the functional (BOLD signals), structural (brain topology) and temporal dimensions of the BOLD time-series for the whole population, and for each condition (ASD and NT).

2.4.2. Finding a discriminative subspace through FKT

After computing a representative matrix that captures the graph spectral components of the BOLD signals for each category, we need to classify the subjects in one of the two categories. In order to do that, we follow an approach inspired by FKT, which allows us to find a discriminative subspace in order to project the GFT coefficients of the BOLD signals. A similar approach is followed by [Subbaraju et al. \(2017\)](#).

First, we need to decorrelate the data by means of a whitening operator. Then, we have to find a transform which keeps the overall effect of *whitening* (step 1), while making the variance of the classes emerge in a complementary way. These operations constitute the simultaneous diagonalization of the joint expectancy matrices $(\bar{S}, \bar{S}^A, \bar{S}^N)$, which are actually related by Eq. 8. In this case, because of the column-wise normalization of the GFT coefficients, \bar{S} has a zero eigenvalue (cf. Appendix A.2), which means the inverse matrix does not exist. Therefore, the whitening matrix, as defined by relation (3), cannot be computed. To circumvent this issue, we propose an extension of the FKT, based on the Newcomb's theorem (cf. Appendix A.3) for the *simultaneous diagonalization* (step 2) of real, symmetric, positive semi-definite matrices. This allows to *compute the final projection matrix* (step 3). The overall approach is thus applied in three steps that we describe in mathematical detail below.

. **Whitening.** Let us consider the eigen-decomposition of the matrix \bar{S} :

$$\mathbf{Q}^T \bar{\mathbf{S}} \mathbf{Q} = \mathbf{\Lambda} \quad \Leftrightarrow \quad \bar{\mathbf{S}} = \mathbf{Q} \mathbf{\Lambda} \mathbf{Q}^T.$$

As $\bar{\mathbf{S}}$ is symmetric, it holds that $\mathbf{Q}^{-1} = \mathbf{Q}^T$. We consider, without loss of generality, that the eigenvalues of $\bar{\mathbf{S}}$ are sorted in ascend order, thus $\Lambda_{11} = 0$. Indeed, we recall that \bar{S} has a zero eigenvalue because of the column-wise normalization of the GFT coefficients used to compute the joint-expectancy matrix $\bar{\mathbf{S}}$. We then define the diagonal matrix $\mathbf{\Gamma}$ such that:

$$\Gamma_{11} = 1 \quad \text{and} \quad \Gamma_{ii} = \Lambda_{ii}^{-1/2}, \quad \text{with } i = 2, \dots, r.$$

Thus, if we set $\mathbf{Q}_2 = \mathbf{\Gamma}^T \mathbf{Q}^T$, we have:

$$\mathbf{Q}_2 \bar{\mathbf{S}} \mathbf{Q}_2^T = \text{diagonal}[\mathbf{0}, \mathbf{I}_{r-1}].$$

where $\text{diagonal}[\mathbf{0}, \mathbf{I}_{r-1}]$ is a diagonal matrix whose first diagonal element is 0 and the $r - 1$ remaining ones equal to one. Using the above developments, Eq. 8 is rewritten as:

$$\begin{aligned} \mathbf{Q}_2 \bar{\mathbf{S}} \mathbf{Q}_2^T &= \alpha_A \mathbf{Q}_2 \bar{\mathbf{S}} \mathbf{Q}_2^T + \alpha_N \mathbf{Q}_2 \bar{\mathbf{S}}^N \mathbf{Q}_2^T \\ \Leftrightarrow \text{diagonal}[\mathbf{0}, \mathbf{I}_{r-1}] &= \alpha_A \bar{\mathbf{S}}^A + \alpha_N \bar{\mathbf{S}}^N. \end{aligned} \quad (9)$$

. **Simultaneous diagonalization of the whitened matrices.** We can show that $\bar{S}^{A'}$ is positive semi-definite (*psd*) and has the following structure (cf. [Appendix A.4](#)):

$$\bar{S}^{A'} = \begin{bmatrix} 0 & \dots & 0 \\ \vdots & \boxed{\bar{S}_{r-1}^{A'}} & \\ 0 & & \end{bmatrix}.$$

In order to diagonalize $\bar{S}^{A'}$, [Newcomb \(1961\)](#) proposes to diagonalize $\bar{S}_{r-1}^{A'}$ by an orthogonal transformation \mathbf{T}' that we deduce through eigen-decomposition. The global transformation matrix \mathbf{T}_2 constitutes of the following:

$$\mathbf{T}_2 = \left[\begin{array}{c|ccc} 1 & 0 & \dots & 0 \\ \hline 0 & & & \\ \vdots & & \mathbf{T}' & \\ 0 & & & \end{array} \right].$$

Thus, $\mathbf{T}_2^T \bar{S}^{A'} \mathbf{T}_2 = \bar{S}^{A''}$, where $\bar{S}^{A''}$ is a diagonal matrix. Eq. 9 can be reformulated as:

$$\begin{aligned} \mathbf{T}_2^T \text{diagonal}[\mathbf{0}, \mathbf{I}_{r-1}] \mathbf{T}_2 &= \alpha_A \mathbf{T}_2^T \bar{S}^{A'} \mathbf{T}_2 + \alpha_N \mathbf{T}_2^T \bar{S}^{N'} \mathbf{T}_2 \\ \Leftrightarrow \text{diagonal}[\mathbf{0}, \mathbf{I}_{r-1}] &= \alpha_A \bar{S}^{A''} + \alpha_N \bar{S}^{N''} \end{aligned}$$

Given that $\text{diagonal}[\mathbf{0}, \mathbf{I}_{r-1}]$ and $\bar{S}^{A''}$ are diagonal matrices, $\bar{S}^{N''}$ is diagonalizable, and it shares the same eigenvectors with $\bar{S}^{A''}$. The non-zero eigenvalues of $\bar{S}^{A''}$ and $\bar{S}^{N''}$, multiplied respectively by α_A and α_N , are complementary and sum to unity.

. **Computation of the projection matrix.** All the above operations can be summarized through a final projection matrix \mathbf{P} such that:

$$\begin{aligned} \mathbf{P} \bar{S} \mathbf{P}^T &= \alpha_A \mathbf{P} \bar{S}^A \mathbf{P}^T + \alpha_N \mathbf{P} \bar{S}^N \mathbf{P}^T \\ \Leftrightarrow \text{diagonal}[\mathbf{0}, \mathbf{I}_{r-1}] &= \alpha_A \bar{S}^{A''} + \alpha_N \bar{S}^{N''}. \end{aligned}$$

with

$$\mathbf{P} = \mathbf{T}_2^T \mathbf{Q}_2 = \mathbf{T}_2^T \mathbf{\Gamma}^T \mathbf{Q}^T. \quad (10)$$

Thus, we end up with a matrix which can be used to project each patient’s matrix of time-varying GFT coefficients in a space where the ASD and NT classes have complementary mean joint expectancy matrices. This explains why the subspace is discriminative: each class may be expressed through a subset of dimensions along which the variance of the related data is high.

2.4.3. Performing classification

Now that we have computed the discriminative projection matrix, we can use it to classify our GFT coefficients of the BOLD signals. Thus, we project the GFT coefficients into the discriminative matrix \mathbf{P} (see Eq. 10):

$$\mathbf{Z}_i = \mathbf{P} \cdot \mathbf{Y}_i. \quad (11)$$

Classification is then achieved by training a decision tree on the variance of the projected GFT coefficients, as described in the following section. We note that the variance of the elements included in the first row of Z_i does not carry any discriminative information. Indeed, along this first dimension, both classes are associated with a zero eigenvalue (see Eq. 10). This is due to the singularity of the mean joint expectancy matrix (see Eq. 6). Actually, circumventing this issue was achieved at the expense of one discriminative dimension in the final projection space, through a transform which is not orthonormal.

3. Experimental protocol

3.1. Data

In this study, we consider the ABIDE I preprocessed dataset (Di Martino et al., 2014; Craddock et al., 2013). It includes Blood Oxygen Level Dependent (BOLD) signals extracted from fMRI through a preprocessing pipeline which is fully detailed on the web platforms related to the ABIDE collection (Pre-processed Connectomes Project, 2014; Autism Brain Imaging Data Exchange,

2013). The BOLD time-series considered in our work were preprocessed according to the C-PAC pipeline, which involves the following main steps: basic processing, noise signal removal, global regression, band-pass filtering (0.01-0.1 Hz), registration, time-series extraction (Preprocessed Connectomes Project, 2014). The selected mean time-series correspond to the Automated Anatomical Labeling atlas on 90 regions of interest, i.e., AAL90 (Tzourio-Mazoyer et al., 2002).

Though exhaustive, the ABIDE dataset presents a high degree of heterogeneity, mainly because of the conditions under which the fMRI acquisition was operated (i.e., eyes closed/opened) as well as the demographic distribution. Thus, to ensure consistent and reliable results, we considered patients who meet the following inclusion criteria:

- eyes opened during fMRI acquisition;
- less than 18 years old;
- less than 0.2 mm in mean framewise displacement.

The corresponding data subset consists of a total of 452 subjects, with respectively 251 neurotypical and 201 ASD subjects.

3.2. Brain topology definition

As discussed in Sec. 2.2, we define the brain graph topology by following a nearest neighbor strategy. In particular, we focus on a two-nearest neighbor topology, which drew our attention in terms of spatial distribution of the ROIs. Indeed, this topology roughly divides the brain in two parts: the fronto-temporal areas on the one side, and the parieto-occipital areas on the other side (see Fig. 2)¹. This choice of topology is meaningful from the neuroscience point of view. Fronto-temporal areas have been associated to dysfunctions and structural

¹Note that the figures presented in this paper were drawn with the BRAINNET SOFTWARE (Xia et al., 2013). The notations and the corresponding ROIs are provided in Appendix A.5.

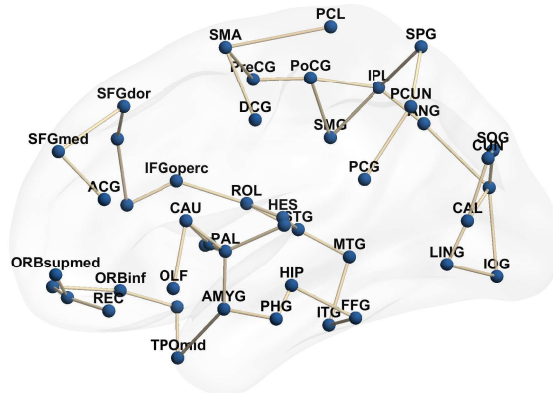


Figure 2: Two-nearest neighbor topology, in the right hemisphere.

abnormalities in ASD subjects (Hirata et al., 2018; Lauvin et al., 2012; Poustka et al., 2012; Goldberg et al., 1999). Actually, the frontal lobe plays an important role in the regulation of our emotions, as it conditions our personality and our ability in making decisions (Abhang et al., 2016). As far as the temporal lobe is concerned, it is notably involved in processing language and emotion, through the amygdala (Abhang et al., 2016; Baars & Gage, 2010).

3.3. Assessment settings

Fig. 3 presents schematically our experimental protocol. The initial dataset is split into training and test sets. This is achieved by picking randomly a fraction x of the total number of instances to constitute a test set. The remaining part is left for training. We consider ten trials, and report the average test accuracy over these trials. Moreover, we compare our framework with two different approaches: the first is based on the classification of the GFT coefficients (cf. Sec. 2.2) and the second is based on SFM (cf. Sec. 2.3).

As shown in Fig. 3, within each trial, the training data are processed through GFT, SFM and our framework. For each patient, training features are derived from the projected BOLD time-series according to the procedures described below.

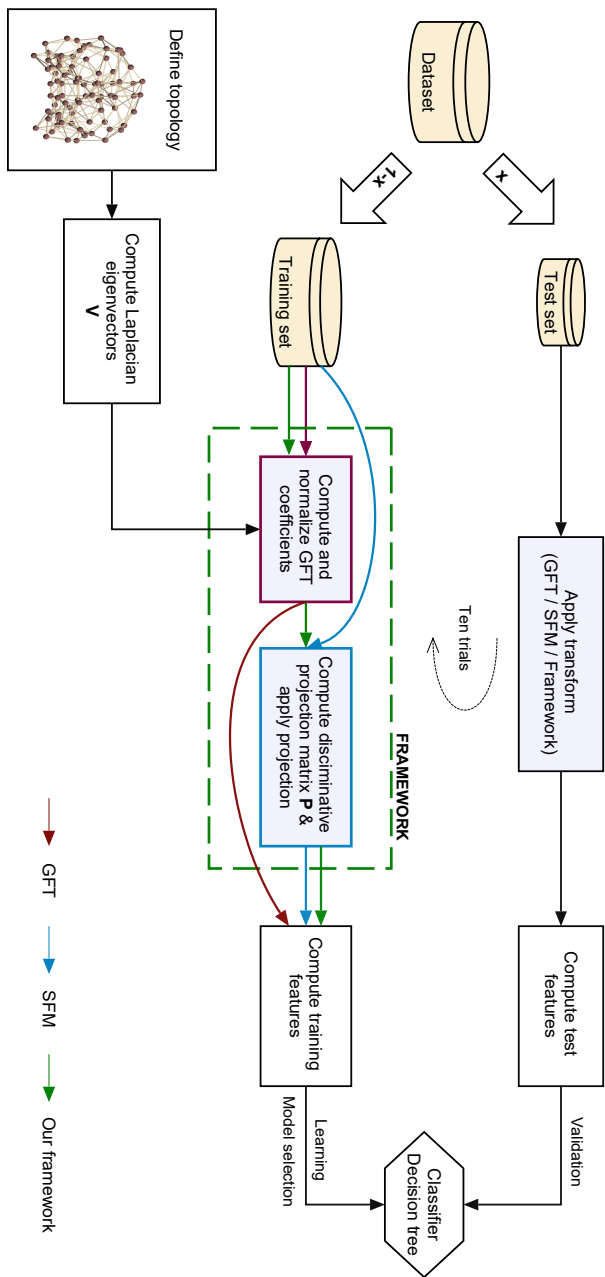


Figure 3: Experimental pipeline

- Concerning the GFT pipeline, we compute the variance of the normalized GFT coefficients (cf. Eq. A.1) over time. As there are 90 ROIs, there are 90 frequency modes, which result in 90 training features per time instance, per subject. We denote the corresponding set of training features as GFT. We also consider the set of variances related to equally-defined frequency bands, i.e., low, middle and high frequency modes. This results in three sets, each including 30 training features : GFT_{LOW} , GFT_{MID} , GFT_{HIGH} . This method has been used for successfully understanding of cognitive flexibility (Medaglia et al., 2018) and motor skill (Huang et al., 2016).
- For both SFM and our framework, we consider the variance of the projected data (cf. respectively Eq. 4 and 11) related to the m most significant dimensions for each group, with $m \in [2, 5]$. Therefore, the total number of training features is $2m$.

3.4. Classifier tuning

In order to classify the subjects into NT and ASD we use a decision tree on the set of training features within each trial. Indeed, this classifier lends itself well to the goal of diagnosis prediction, as it ensures the interpretability of the prediction outputs. In terms of implementation, we consider the C4.5 implementation of WEKA (Frank et al., 2016). All parameters are kept at their default values, except from the minimal number of instances per leaf, which is a parameter conditioning the decision tree depth. The latter is set based on a cross-validation procedure.

4. Results

4.1. Comparison with state-of-the-art methods

Fig. 4 shows the best averaged test accuracies achieved by each method (and each modality), according to the procedure described in Sec. 3.3, for different sizes of the training set (from 95% to 70%, per step of 5%). Overall, our method outperforms both SFM and GFT. As expected, as the training set size decreases,

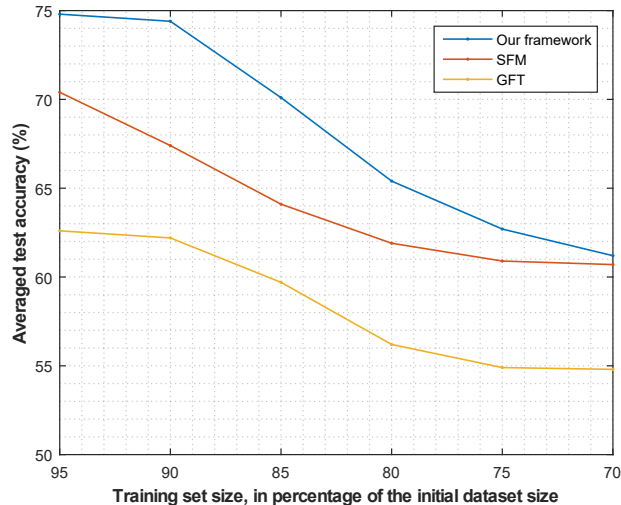


Figure 4: Performances of the methods for different training set sizes

the performance deteriorates significantly for all the methods. We note that both SFM and our method are based on the estimation of a covariance matrix through the sample covariance, which requires a large amount of data. This is particularly true for the ASD population which is quite heterogeneous in profiles, given the extent of the spectrum.

Table 1 presents in detail the averaged test accuracies obtained by keeping 95% of the initial dataset for training, for different assessment modalities. The gain achieved with our framework, which reaches up to 4.4%, indicates that:

- in comparison to SFM, the interplay between the structural and functional connectivity is worth considering to improve prediction;
- in comparison to GFT, it seems that the discriminative information is hidden in more complex patterns, revealed by combining the GFT coefficients.

Finally, we study the interpretability of the features obtained by our framework. Fig. 5 presents the decision tree achieved on the basis of the three most discriminative dimensions ($m = 3$) for each of the two groups. By *ASD_dom*

m	SFM (%)	Ours (%)	Modality	GFT (%)
2	69.1	73.5	GFT	53.9
3	70.4	74.8	GFT _{LOW}	59.6
4	69.6	73.0	GFT _{MID}	62.6
5	67.4	71.3	GFT _{HIGH}	59.1

Table 1: Averaged test accuracy: SFM and our framework

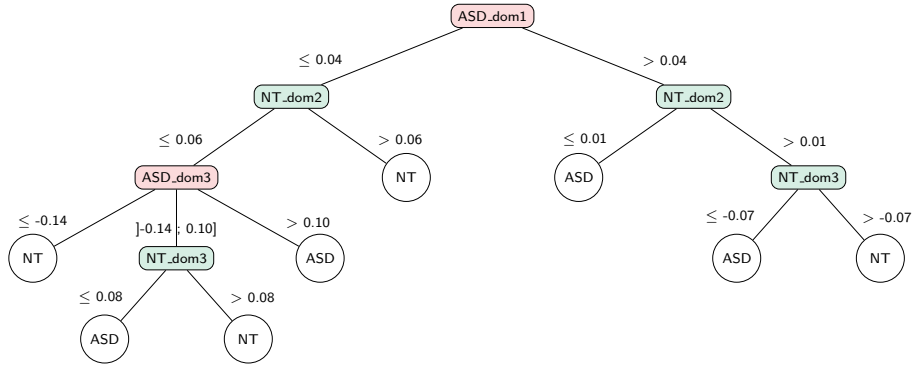


Figure 5: Decision tree based on the projected coefficients of our framework; subdivisions are related to the log-variance values.

m	SFM (%)	Our framework (%)		
		2-NN	FC	UFC
2	69.1	73.5	71.3	66.1
3	70.4	74.8	73.0	69.1
4	69.6	73.0	73.0	65.2
5	67.4	71.3	71.3	63.9

Table 2: Influence of the topology on the predictive performances

(respectively NT_dom) we denote a dimension along which the ASD group (resp. NT group) has a large variance; the number corresponding to this feature refers to the discriminative power of the dimension. For instance, ASD_dom1 (resp. NT_dom1) refers to the first strongly dominant dimension for the ASD group (resp. NT group). The subdivisions are based on the variance (over time) of the coefficients along the dimension in question. More precisely, for a given patient, the decision tree checks the feature corresponding to ASD_dom1 . If the variance along this dimension is high, the algorithm examines the features corresponding to NT_dom2 . A low variance observed along this dimension implies an ASD diagnosis.

4.2. Influence of the topology

In order to understand the influence of the topology on the classification performance, we perform two additional experiments, by considering two alternative connectivity matrices:

- A Fully Connected (FC) topology, which is generated by connecting all the ROIs/nodes of the graph to each other, and assigning the corresponding weights to the connections, as defined in Sec. 2.2.
- An Unweighted Fully Connected (UFC) topology, which is generated by connecting all the ROIs/nodes of the graph to each other and assigning a constant, unit weight to all the connections.

Table 2 presents the predictive performances corresponding to these settings, in comparison to the results achieved with a 2-NN topology. For completeness, we show the results of the SFM method. On the one hand, it is worth noting that the performances achieved with the FC topology are close, but a bit lower than in the case of 2-NN. This is quite promising as it shows that probably the additional edges added to the 2-NN graph, i.e., non-local interactions, are not important. In fact, they add some noise to the process. The performance of the two schemes are relatively close because the weights of these additional edges are small. Indeed, we handle a brain network of 90 nodes in which the distances between the ROIs decrease quickly. On the other hand, the prediction rates achieved with the UFC topology are inferior, but close to the ones of SFM. These results are expected as a UFC topology is similar to the settings of SFM, where the irregular structure is ignored. Thus, these results confirm the importance of the topology.

5. Discussion

The above mentioned results suggest that our framework is efficient in terms of predictive accuracy. Thus, it appears that considering the structure-function interplay is crucial in classifying ASD and NT subjects. This pertinent information is however hidden in discriminative patterns which are made of complex combinations of the graph Fourier modes. The analysis of the projection matrix \mathbf{P} allows us to understand how these combinations are made, and which modes contribute the most to the discriminative features.

From Eq. 11, we notice that the rows of the discriminative matrix \mathbf{P} act as filters on the GFT coefficients contained in each column of matrix \mathbf{Y}_i . The result is a weighted sum of the GFT coefficients in the projection space on each of its dimensions. Figs. 6 and 7 show the values of the matrix \mathbf{P} rows (in absolute values) which correspond to the dimensions considered by the decision tree of Fig. 5.

Fig. 6 is related to the set of weights applied on the GFT coefficients for

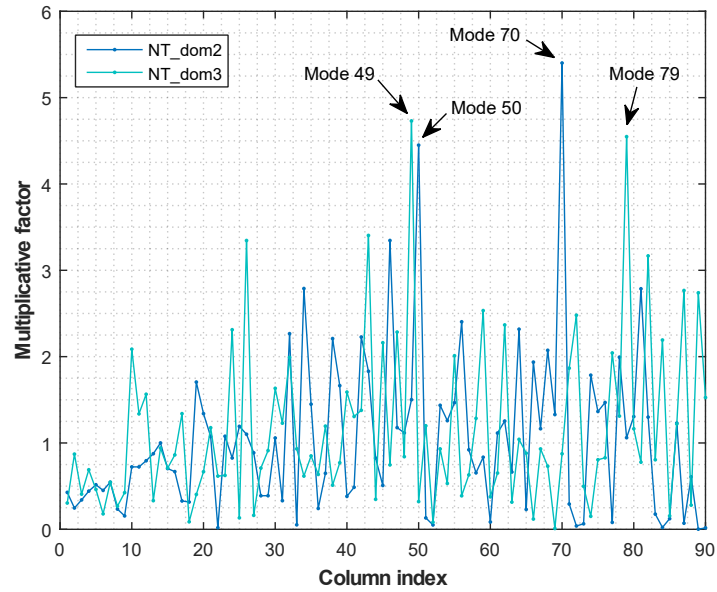


Figure 6: Matrix P: interpretation of the rows – NT-dominant dimensions

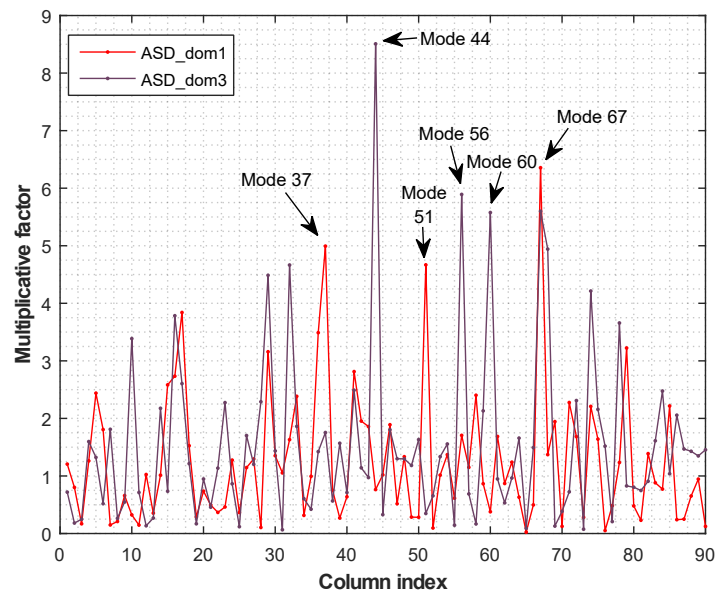


Figure 7: Matrix P: interpretation of the rows – ASD-dominant dimensions

their projection on the NT-dominant dimensions used by the predictive model (see Fig. 5). We notice that some weights are dominant over the others of the same row, i.e., some GFT coefficients are, in terms of absolute values, more amplified than others in the final projection space. This allows to point out the corresponding graph Fourier modes, belonging to different levels of frequency (i.e., low, medium, high), as key patterns for classification, whose corresponding weights are deviating from the mean by more than 2.5 times the standard deviation. The same observation is valid in Fig. 7 for the ASD-dominant dimensions.

Given the above, we are led to an interesting interpretation of the results. Indeed, by computing the variance of the projected GFT coefficients, we actually measure the variability over time of the presence of some graph Fourier modes in the fMRI signals. These modes may be seen as *frequency signatures* of the NT/ASD conditions. This constitutes another difference with the SFM method which allows to point out isolated prominent regions (Subbaraju et al., 2017).

The analysis of the graph Fourier modes pointed out in Fig. 6 reveals three out of the four signatures which correspond to a predominant activity in the parieto-occipital regions (see Fig. 8). Regarding the significant modes of the ASD population which are pointed out in Fig. 7, they are all related to high levels of activity in the fronto-temporal areas in ASD subject (see Fig. 9). This result is consistent with the previous findings reported in the literature of neuroscience concerning the influence of the frontal and temporal lobes in ASD (Hirata et al., 2018; Lauvin et al., 2012; Poustka et al., 2012; Goldberg et al., 1999). The latter constitutes a strong result given (i) the heterogeneity of the samples, (ii) the simplistic definition of the brain topology. Indeed, our sample is heterogeneous by the range of the patients' ages (between 6 and 18 years old) and the range of profiles covered by the ASD spectrum (i.e., Asperger's, Pervasive Developmental Disorder-Not Otherwise Specified, autism). Moreover, as mentioned previously, the topological structure that we considered is only an approximation of the brain structural connectivity.

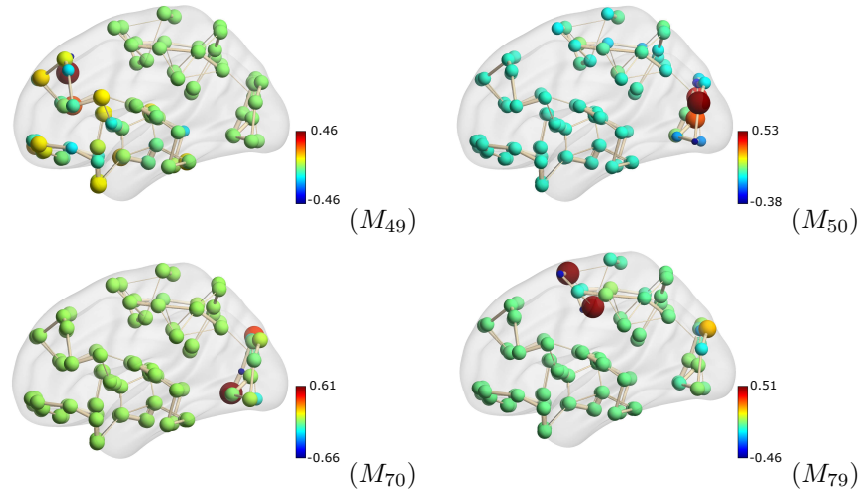


Figure 8: Significant frequency Modes (M) in NT patients

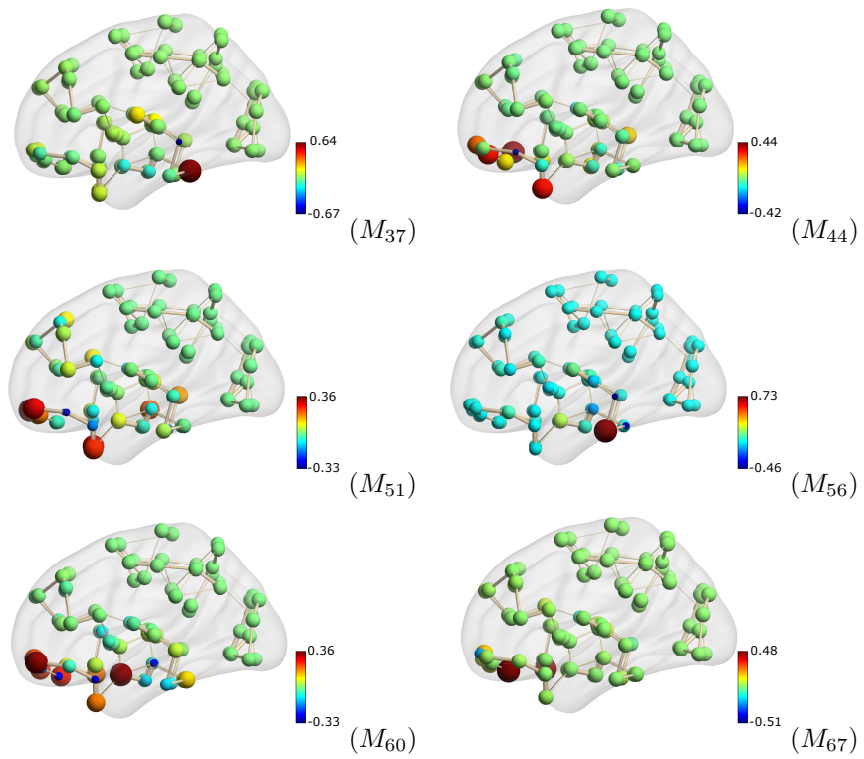


Figure 9: Significant frequency Modes (M) in ASD

6. Conclusion

In this work, we proposed a framework that exploits the structure (brain topology)-function (fMRI-based activity) interplay of the brain to predict Autism Spectrum Disorder (ASD). In this context, we defined a brain graph as a set of Regions of Interest (ROIs) connected in terms of their topological distance. Through tools borrowed from the field of Graph Signal Processing (GSP), we extracted features related to the frequency content of rs-fMRI signals which reside on the nodes of the brain graph. These features were then processed through an extension of the Fukunaga-Koontz transform to build discriminative markers for the classification of ASD and NeuroTypical (NT) patients.

The approach was applied on the publicly available ABIDE dataset. We summarize below the main conclusions of this study.

- The proposed methodology performed favorably in comparison to state-of-the-art methods, on the basis of a decision tree as a predictive model.
- The analysis of the results reveals the influence of the frontal and temporal lobes in the diagnosis of the disorder. This finding is consistent with previous reports of the literature of neuroscience.
- In terms of brain activity, we show that the neuropathology may not be attributed to impairments in low, medium and high frequency modes. Indeed, we observe the significant involvement of components that are picked in different parts of the frequency spectrum in the creation of the discriminative features.

These findings indicate that exploiting jointly structural and functional information of the brain regions is more efficient than considering each of them separately. We believe that such an approach paves the way for a better understanding of the disease and thus the exploration of new research avenues by medical experts.

7. Acknowledgements

Sarah Itani is a research fellow of the F.R.S.-FNRS. We thank Professors Philippe Fortemps, Arnaud Vandaele, Fabian Lecron (Faculty of Engineering, University of Mons), Professor Mandy Rossignol (Faculty of Psychology and Education, University of Mons, Belgium), Dr. Xiaowen Dong (University of Oxford), and Dr. Christine Choirat (Swiss Data Science Center - EPFL and ETH Zurich) for their advice and interest in this work.

Appendix A. Appendices

Appendix A.1. The pair-wise joint expectancy is semi-definite positive

We can prove that the pair-wise joint expectancy \mathbf{S}_i , as defined by relation (5), is positive semi-definite. For simplicity, we ignore the index i . By definition, a matrix \mathbf{S} is positive semi-definite if:

$$x^T \mathbf{S} x \geq 0 \quad \forall x \in \mathbb{R}^n.$$

In this case, $\mathbf{S} = \mathbf{Y}\mathbf{Y}^T$, which involves, $\forall x \in \mathbb{R}^n$:

$$x^T \mathbf{S} x = x^T \mathbf{Y}\mathbf{Y}^T x = (\mathbf{Y}^T x)^T (\mathbf{Y}^T x) = \|\mathbf{Y}^T x\|^2 \geq 0.$$

Appendix A.2. The mean pair-wise joint expectancy is non invertible

Let us express the matrix \mathbf{Y}_i of normalized GFT coefficients for a given patient i as:

$$\mathbf{Y}_i = (\hat{\mathbf{X}}_i - \mathbf{M}_i) \cdot \mathbf{R}_i \quad \text{with} \quad \mathbf{M}_i = \mathbf{U}\mathbf{V}^T \mathbf{X}_i \quad (\text{A.1})$$

where \mathbf{R}_i is a diagonal matrix including the norm of the columns of \mathbf{Y}_i and \mathbf{M}_i is a matrix including the mean of the columns of $\hat{\mathbf{X}}_i$; \mathbf{U} is a $r \times r$ constant matrix including entries equal to $1/r$.

Given (A.1), an alternative expression for the mean joint expectancy matrix $\bar{\mathbf{S}}$ is:

$$\bar{\mathbf{S}} = \frac{1}{n} \sum_i (\hat{\mathbf{X}}_i - \mathbf{M}_i) \cdot \mathbf{H}_i \cdot (\hat{\mathbf{X}}_i - \mathbf{M}_i)^T.$$

where, for the sake of simplicity, we denote \mathbf{H}_i as:

$$\frac{\mathbf{D}_i^2}{\text{Tr}(\mathbf{Y}_i \mathbf{Y}_i^T)}.$$

The matrix $\bar{\mathbf{S}}$ has a zero eigenvalue associated to a constant eigenvector, that is, if q denotes a constant column vector:

$$\bar{\mathbf{S}}q = 0.$$

*** *Proof*

$$\bar{\mathbf{S}}q = \frac{1}{n} \sum_i (\hat{\mathbf{X}}_i - \mathbf{M}_i) \cdot \mathbf{H}_i \cdot (\hat{\mathbf{X}}_i^T - \mathbf{M}_i^T) \cdot q \quad (\text{A.2})$$

Let us focus on the individual terms, i.e., for each i :

$$\begin{aligned} & (\hat{\mathbf{X}}_i - \mathbf{M}_i) \cdot \mathbf{H}_i \cdot (\hat{\mathbf{X}}_i^T - \mathbf{M}_i^T) \cdot q \\ &= \hat{\mathbf{X}}_i \mathbf{H}_i \hat{\mathbf{X}}_i^T q - \hat{\mathbf{X}}_i \mathbf{H}_i \mathbf{M}_i^T q - \mathbf{M}_i \mathbf{H}_i \hat{\mathbf{X}}_i^T q + \mathbf{M}_i \mathbf{H}_i \mathbf{M}_i^T q. \end{aligned} \quad (\text{A.3})$$

Yet $\hat{\mathbf{X}}_i^T q = \mathbf{M}_i^T q$. Indeed:

$$\begin{aligned} \mathbf{M}_i^T q &= (\mathbf{U} \mathbf{V}^T \cdot \mathbf{X}_i)^T q \\ &= (\mathbf{V}^T \cdot \mathbf{X}_i)^T \mathbf{U}^T q \\ &= \hat{\mathbf{X}}_i^T \mathbf{U}^T q. \end{aligned}$$

As \mathbf{U} is a square constant matrix, $\mathbf{U}^T = \mathbf{U}$. The vector $\mathbf{U}q$ includes the mean of each element of the vector q , which is a constant vector. Thus $\mathbf{U}q = q$ and

$$\mathbf{M}_i^T q = \hat{\mathbf{X}}_i^T q$$

which means that (A.3) sums to zero and thus, (A.2) also. This is related to the mean centering operation, executed over the columns of the matrices $\hat{\mathbf{X}}_i$. ***

Appendix A.3. The theorem of Newcomb

For the sake of completeness, we recall here the main results of the theorem.

Diagonalization (Newcomb, 1961). Let \mathbf{A} and \mathbf{B} be $n \times n$ real, symmetric, positive semi-definite matrices. Then there exists a real non-singular matrix \mathbf{T} and real diagonal matrices \mathbf{A}_0 and \mathbf{B}_0 such that

$$\begin{aligned}\mathbf{A} &= \mathbf{T}\mathbf{A}_0\mathbf{T}^T \\ \mathbf{B} &= \mathbf{T}\mathbf{B}_0\mathbf{T}^T\end{aligned}$$

where

$$\mathbf{A}_0 = \text{diagonal}[\mathbf{0}_{n-\mathbf{a}}, \mathbf{I}_{\mathbf{a}}]$$

if \mathbf{a} denotes the rank of matrix \mathbf{A} .

Appendix A.4. Positive semi-definiteness and structure of $\bar{\mathbf{S}}^{\mathbf{A}'}$

By definition, as the matrix of joint expectancy $\bar{\mathbf{S}}^{\mathbf{A}}$ is positive semi-definite (*psd*), we have:

$$x^T \bar{\mathbf{S}}^{\mathbf{A}} x \geq 0 \quad \forall x \in \mathbb{R}^n. \quad (\text{A.4})$$

We can show that $\bar{\mathbf{S}}^{\mathbf{A}'}$ is *psd* as well. Indeed, let us set $x = \mathbf{Q}_2^T y$, $\forall y \in \mathbb{R}^n$. Then:

$$\begin{aligned}y^T \bar{\mathbf{S}}^{\mathbf{A}'} y &= y^T \mathbf{Q}_2 \bar{\mathbf{S}}^{\mathbf{A}} \mathbf{Q}_2^T y = (\mathbf{Q}_2^T y)^T \bar{\mathbf{S}}^{\mathbf{A}} (\mathbf{Q}_2^T y) \\ &= x^T \bar{\mathbf{S}}^{\mathbf{A}} x \geq 0\end{aligned}$$

which involves $y^T \bar{\mathbf{S}}^{\mathbf{A}'} y \geq 0 \Rightarrow \bar{\mathbf{S}}^{\mathbf{A}'} \succeq 0$. By adopting a similar reasoning, we can show that $\bar{\mathbf{S}}^{\mathbf{N}'}$ is also *psd*.

As a *psd* matrix, the diagonal entries of $\bar{\mathbf{S}}^{\mathbf{A}'}$ are positive (Golub & Van Loan, 2012). Thus, to satisfy (9), the first main diagonal entry of $\bar{\mathbf{S}}^{\mathbf{A}'}$ (resp. $\bar{\mathbf{S}}^{\mathbf{N}'}$) must be equal to zero; the corresponding row and column are zero, given the *psd-ness* of $\bar{\mathbf{S}}^{\mathbf{A}'}$ (resp. $\bar{\mathbf{S}}^{\mathbf{N}'}$) (Horn et al., 1990; Golub & Van Loan, 2012).

Appendix A.5. Brain figures

Table A.3 lists the ROIs of the AAL atlas grouped by partition, as suggested by Wang et al. (2012). These ROIs are labeled with the notations proposed by

the BRAINNET SOFTWARE, which was used to draw the brain figures. The ROI indexes related to the AAL atlas are also provided: odd (even) numbers refer to left (right) ROI.

References

- Abhang, P. A., Gawali, B. W., & Mehrotra, S. C. (2016). *Introduction to EEG- and Speech-Based Emotion Recognition*. Academic Press.
- Alexander-Bloch, A. F., Vertes, P. E., Stidd, R., Lalonde, F., Clasen, L.,
5 Rapoport, J., Giedd, J., Bullmore, E. T., & Gogtay, N. (2012). The anatomical distance of functional connections predicts brain network topology in health and schizophrenia. *Cerebral cortex*, *23*, 127–138.
- Autism Brain Imaging Data Exchange (2013). Welcome to the Autism Brain Imaging Data Exchange! http://fcon_1000.projects.nitrc.org/indi/abide/.
10 [Online; accessed 03-11-2018].
- Autism Speaks (2018). DSM-5 Criteria. <https://www.autismspeaks.org/dsm-5-criteria>. [Online; accessed 02-11-2018].
- Baars, B. J., & Gage, N. M. (2010). *Cognition, brain, and consciousness: Introduction to cognitive neuroscience*. Academic Press.
- 15 Bullmore, E., & Sporns, O. (2009). Complex brain networks: graph theoretical analysis of structural and functional systems. *Nature Reviews Neuroscience*, *10*, 186–198.
- Chen, H., Duan, X., Liu, F., Lu, F., Ma, X., Zhang, Y., Uddin, L. Q., & Chen, H. (2016). Multivariate classification of autism spectrum disorder using
20 frequency-specific resting-state functional connectivitya multi-center study. *Progress in Neuro-Psychopharmacology and Biological Psychiatry*, *64*, 1–9.
- Cheng, W., Rolls, E. T., Zhang, J., Sheng, W., Ma, L., Wan, L., Luo, Q., & Feng, J. (2017). Functional connectivity decreases in autism in emotion, self, and

PARTITION	INDEX L-R	ROI	LABEL
Frontal	03-04	Frontal_Sup	SFGdor
	05-06	Frontal_Sup_Orb	ORBsup
	07-08	Frontal_Mid	MFG
	09-10	Frontal_Mid_Orb	ORBmid
	11-12	Frontal_Inf_Oper	IFGoperc
	13-14	Frontal_Inf_Tri	IFGtriang
	15-16	Frontal_Inf_Orb	ORBinf
	23-24	Frontal_Sup_Medial	SFGmed
	25-26	Frontal_Med_Orb	ORBsupmed
	27-28	Rectus	REC
Parietal	01-02	Precentral	PreCG
	19-20	Supp_Motor_Area	SMA
	57-58	Postcentral	PoCG
	59-60	Parietal_Sup	SPG
	61-62	Parietal_Inf	IPL
	63-64	SupraMarginal	SMG
	65-66	Angular	ANG
	67-68	Precuneus	PCUN
	69-70	Paracentral_Lobule	PCL
Occipital	43-44	Calcarine	CAL
	45-46	Cuneus	CUN
	47-48	Lingual	LING
	49-50	Occipital_Sup	SOG
	51-52	Occipital_Mid	MOG
	53-54	Occipital_Inf	IOG
	55-56	Fusiform	FFG
Temporal	17-18	Rolandic_Operr	ROL
	29-30	Insula	INS
	37-38	Hippocampus	HIP
	39-40	ParaHippocampal	PHG
	41-42	Amygdala	AMYG
	79-80	Heschl	HES
	81-82	Temporal_Sup	STG
	83-84	Temporal_Pole_Sup	TPOsup
	85-86	Temporal_Mid	MTG
	87-88	Temporal_Pole_Mid	TPOmid
89-90	Temporal_Inf	ITG	
Cingulum	31-32	Cingulum_Ant	ACG
	33-34	Cingulum_Mid	DCG
	35-36	Cingulum_Post	PCG
Subcortical	21-22	Olfactory	OLF
	71-72	Caudate	CAU
	73-74	Putamen	PUT
	75-76	Pallidum	PAL
	77-78	Thalamus	THA

Table A.3: AAL atlas (Xia et al., 2013; Wang et al., 2012; Tzourio-Mazoyer et al., 2002)

- face circuits identified by knowledge-based enrichment analysis. *Neuroimage*,
25 148, 169–178.
- Craddock, C., Benhajali, Y., Chu, C., Chouinard, F., Evans, A., Jakab, A.,
Khundrakpam, B. S., Lewis, J. D., Li, Q., Milham, M. et al. (2013). The Neuro
Bureau preprocessing initiative: open sharing of preprocessed neuroimaging
data and derivatives. *Neuroinformatics*, .
- 30 Di Martino, A., Yan, C.-G., Li, Q., Denio, E., Castellanos, F. X., Alaerts, K.,
Anderson, J. S., Assaf, M., Bookheimer, S. Y., Dapretto, M. et al. (2014).
The autism brain imaging data exchange: towards large-scale evaluation of
the intrinsic brain architecture in autism. *Molecular psychiatry*, 19, 659.
- Doshi-Velez, F., & Kim, B. (2017). A roadmap for a rigorous science of inter-
35 pretability. In *arXiv preprint arXiv:1702.08608*.
- Frank, E., Hall, M. A., & Witten, I. H. (2016). *The WEKA Workbench. Online
Appendix for "Data Mining: Practical Machine Learning Tools and Tech-
niques"*. Morgan Kaufmann.
- Fukunaga, K. (2013). *Introduction to statistical pattern recognition*. Elsevier.
- 40 Fukunaga, K., & Koontz, W. L. (1970). Application of the karhunen-loeve
expansion to feature selection and ordering. *IEEE Transactions on computers*,
100, 311–318.
- Goch, C. J., Oztan, B., Stieltjes, B., Henze, R., Hering, J., Poustka, L., Meinzer,
H.-P., Yener, B., & Maier-Hein, K. H. (2014). Global changes in the connec-
45 tome in autism spectrum disorders. In *Computational Diffusion MRI and
Brain Connectivity* (pp. 239–247). Springer.
- Goldberg, M., Mena, I., & Miller, B. (1999). Frontal and temporal lobe dysfunc-
tion in autism and other related disorders: Adhd and ocd. *Latin American
Journal of Nuclear Medicine*, .

- 50 Golub, G. H., & Van Loan, C. F. (2012). *Matrix computations* volume 3. JHU Press.
- Hirata, K., Egashira, K., Harada, K., Nakashima, M., Hirotsu, M., Isomura, S., Watanuki, T., Matsubara, T., Kaku, Y., Kaneyuki, H. et al. (2018). Differences in frontotemporal dysfunction during social and non-social cognition
55 tasks between patients with autism spectrum disorder and schizophrenia. *Scientific reports*, 8, 3014.
- Horn, R. A., Horn, R. A., & Johnson, C. R. (1990). *Matrix analysis*. Cambridge university press.
- Huang, W., Goldsberry, L., Wymbs, N. F., Grafton, S. T., Bassett, D. S., &
60 Ribeiro, A. (2016). Graph frequency analysis of brain signals. *J. Sel. Topics Signal Processing*, 10, 1189–1203.
- Itani, S., Lecron, F., & Fortemps, P. (2019). Specifics of medical data mining for diagnosis aid: A survey. *Expert Systems with Applications*, 118, 300–314.
- Kana, R. K., Uddin, L. Q., Kenet, T., Chugani, D., & Müller, R.-A. (2014).
65 Brain connectivity in autism. *Frontiers in Human Neuroscience*, 8, 349.
- Kassraian-Fard, P., Matthis, C., Balsters, J. H., Maathuis, M. H., & Wenderoth, N. (2016). Promises, pitfalls, and basic guidelines for applying machine learning classifiers to psychiatric imaging data, with autism as an example. *Frontiers in psychiatry*, 7, 177.
- 70 Ktena, S. I., Parisot, S., Ferrante, E., Rajchl, M., Lee, M., Glocker, B., & Rueckert, D. (2018). Metric learning with spectral graph convolutions on brain connectivity networks. *NeuroImage*, 169, 431–442.
- Lauvin, M.-A., Martineau, J., Destrieux, C., Andersson, F., Bonnet-Brilhault, F., Gomot, M., El-Hage, W., & Cottier, J.-P. (2012). Functional morpho-
75 logical imaging of autism spectrum disorders: current position and theories proposed. *Diagnostic and interventional imaging*, 93, 139–147.

- Maximo, J. O., Cadena, E. J., & Kana, R. K. (2014). The implications of brain connectivity in the neuropsychology of autism. *Neuropsychology review*, *24*, 16–31.
- 80 Medaglia, J. D., Huang, W., Karuza, E. A., Kelkar, A., Thompson-Schill, S. L., Ribeiro, A., & Bassett, D. S. (2018). Functional alignment with anatomical networks is associated with cognitive flexibility. *Nature Human Behaviour*, *2*, 156.
- Mueller, S., Keeser, D., Samson, A. C., Kirsch, V., Blautzik, J., Grothe, M.,
85 Erat, O., Hegenloh, M., Coates, U., Reiser, M. F. et al. (2013). Convergent findings of altered functional and structural brain connectivity in individuals with high functioning autism: a multimodal MRI study. *PloS one*, *8*, e67329.
- Nair, A., Treiber, J. M., Shukla, D. K., Shih, P., & Müller, R.-A. (2013). Impaired thalamocortical connectivity in autism spectrum disorder: a study of
90 functional and anatomical connectivity. *Brain*, *136*, 1942–1955.
- Newcomb, R. W. (1961). On the simultaneous diagonalization of two semi-definite matrices. *Quarterly of Applied Mathematics*, *19*, 144–146.
- Ortega, A., Frossard, P., Kovačević, J., Moura, J. M., & Vandergheynst, P. (2018). Graph signal processing: Overview, challenges, and applications.
95 *Proceedings of the IEEE*, *106*, 808–828.
- Poustka, L., Jennen-Steinmetz, C., Henze, R., Vomstein, K., Haffner, J., & Sieltjes, B. (2012). Fronto-temporal disconnectivity and symptom severity in children with autism spectrum disorder. *The World Journal of Biological Psychiatry*, *13*, 269–280.
- 100 Preprocessed Connectomes Project (2014). ABIDE Preprocessed. <http://preprocessed-connectomes-project.org/abide/>. [Online; accessed 03-11-2018].

- Rane, P., Cochran, D., Hodge, S. M., Haselgrove, C., Kennedy, D., & Frazier, J. A. (2015). Connectivity in autism: a review of MRI connectivity studies. *Harvard review of psychiatry*, *23*, 223.
105
- Ray, S., Miller, M., Karalunas, S., Robertson, C., Grayson, D. S., Cary, R. P., Hawkey, E., Painter, J. G., Kriz, D., Fombonne, E. et al. (2014). Structural and functional connectivity of the human brain in autism spectrum disorders and attention-deficit/hyperactivity disorder: a rich club-organization study. *Human brain mapping*, *35*, 6032–6048.
110
- Shuman, D. I., Narang, S. K., Frossard, P., Ortega, A., & Vandergheynst, P. (2013). The emerging field of signal processing on graphs: Extending high-dimensional data analysis to networks and other irregular domains. *IEEE Signal Processing Magazine*, *30*, 83–98.
- 115 Sporns, O. (2013). Structure and function of complex brain networks. *Dialogues in clinical neuroscience*, *15*, 247.
- Subbaraju, V., Suresh, M. B., Sundaram, S., & Narasimhan, S. (2017). Identifying differences in brain activities and an accurate detection of autism spectrum disorder using resting state functional-magnetic resonance imaging: A spatial filtering approach. *Medical image analysis*, *35*, 375–389.
120
- Tolan, E., & Isik, Z. (2018). Graph theory based classification of brain connectivity network for autism spectrum disorder. In *International Conference on Bioinformatics and Biomedical Engineering* (pp. 520–530). Springer.
- Tzourio-Mazoyer, N., Landeau, B., Papathanassiou, D., Crivello, F., Etard, O., Delcroix, N., Mazoyer, B., & Joliot, M. (2002). Automated anatomical labeling of activations in SPM using a macroscopic anatomical parcellation of the MNI MRI single-subject brain. *Neuroimage*, *15*, 273–289.
125
- Uddin, L. Q., Supekar, K., & Menon, V. (2013). Reconceptualizing functional brain connectivity in autism from a developmental perspective. *Frontiers in human neuroscience*, *7*, 458.
130

- Vissers, M. E., Cohen, M. X., & Geurts, H. M. (2012). Brain connectivity and high functioning autism: a promising path of research that needs refined models, methodological convergence, and stronger behavioral links. *Neuroscience & Biobehavioral Reviews*, *36*, 604–625.
- 135 Von Luxburg, U. (2007). A tutorial on spectral clustering. *Statistics and computing*, *17*, 395–416.
- Wang, J., Calhoun, V. D., Stephen, J. M., Wilson, T. W., & Wang, Y.-p. (2018). Integration of network topological features and graph Fourier transform for fMRI data analysis. In *Biomedical Imaging (ISBI 2018), 2018 IEEE 15th International Symposium on* (pp. 92–96). IEEE.
- 140 Wang, Z., Liu, J., Zhong, N., Qin, Y., Zhou, H., & Li, K. (2012). Changes in the brain intrinsic organization in both on-task state and post-task resting state. *Neuroimage*, *62*, 394–407.
- Xia, M., Wang, J., & He, Y. (2013). BrainNet Viewer: a network visualization
145 tool for human brain connectomics. *PloS one*, *8*, e68910.